

Haptic Simulator for Prostate Brachytherapy with Simulated Needle and Probe Interaction

Orcun Goksel, *Member, IEEE*, Kirill Sapchuk, *Student Member, IEEE*, and Septimiu E. Salcudean, *Fellow, IEEE*

Abstract—This paper presents a haptic simulator for prostate brachytherapy. Both needle insertion and the manipulation of the transrectal ultrasound (TRUS) probe are controlled via haptic devices. Tissue interaction forces that are computed by a deformable tissue model based on the finite element method (FEM) are rendered to the user by these devices. The needle insertion simulation employs 3D models of needle flexibility and asymmetric tip bevel. The needle-tissue simulation allows a trainee to practice needle insertion and targeting. The TRUS-tissue interaction simulation allows a trainee to practice the 3D intraoperative TRUS placement for registration with the preoperative volume study and to practice TRUS axial translation and rotation for imaging needles during insertions. Approaches to computational acceleration for realtime haptic performance are presented. Trade-offs between accuracy and speed are discussed. A graphics-card implementation of the numerically intensive mesh-adaptation operation is also presented. The simulator can be used for training, rehearsal, and treatment planning.

Index Terms—Medical training, prostate brachytherapy.

1 INTRODUCTION

PROSTATE brachytherapy is an effective treatment for early-stage locally confined prostate cancer. It involves the permanent implantation of radioactive seeds in and around the prostate under the image guidance of transrectal ultrasound (TRUS). In brachytherapy, a large number (80–130) of radioactive sources or seeds are delivered using long, flexible needles as seen in Fig. 1. Twenty-to-twenty five needles are inserted through a *template* according to a plan that is prepared based on a TRUS prostate volume study, which is acquired a few weeks prior to the procedure. Accordingly, at the beginning of the procedure, the TRUS probe is manipulated until the prostate images observed match the ones collected during the planning volume study. This ensures a probe placement with respect to the prostate similar to that in the planning study, thereby aligning the template to its planned position. Subsequently, each needle is inserted through its planned template grid hole to a corresponding planned depth to deposit the seeds. See [1] for a detailed description of this procedure.

Seed placement errors may lead to an undesired radioactive dose distribution, causing complications such as incontinence and impotence and degrading the quality of life of patients. Medical residents commonly acquire the necessary brachytherapy skills in the operating room under the supervision of an expert physician. Having identified the need for alternative training methods for prostate brachytherapy, a haptic interaction simulation is presented

in this paper offering a computational environment for medical personnel training and procedure rehearsal.

Due to pubic arch interference, prostate swelling, the state of bladder fullness, patient positioning, and other factors, it is common for the physician to adjust the TRUS probe during the procedure in order to realign the plan to preoperative images and make other minor adjustments to seed implant locations, as necessary, in order to improve dose administration. Consequently, the TRUS probe and the needles are the two medical instruments that interact with the patient's anatomy during prostate brachytherapy and hence need to be modeled for a complete simulation environment. This paper studies the development of a haptic interaction model between both these instruments and a deformable tissue representation of the anatomy.

Haptic medical simulations have been extensively investigated as a training tool, especially in the context of minimally invasive surgery [2]. There are commercial haptic simulators for laparoscopy, endoscopy, and endovascular procedures [3], [4]. The modeling of soft tissue deformation has also received significant attention from the research community. Various modeling techniques have been proposed, a review of which is presented in [5]. With advances in computational hardware, the use of the finite element method (FEM) for tissue deformation has become a de facto standard due to its physically based continuum mechanics representation. Modeling the interaction of medical tools with deformable tissue has been studied extensively [6].

Needle insertion modeling, in particular, has been of interest to many researchers, with different approaches having been presented, see [7] for a review. These aim to address two aspects of needle insertion: 1) modeling forces during needle insertions [8], [9], [10], [11], [12] and 2) modeling the needle path [13], [14], [15]. Considering the former, needle forces were investigated *in vitro* using force sensors [8]. Force models and parameterizations were also proposed from phantom experiments where displacements were observed using, for example, photographic [9],

• The authors are with the Department of Electrical and Computer Engineering, University of British Columbia, Vancouver, BC, Canada. E-mail: {orcung, tims}@ece.ubc.ca, ksapchuk@gmail.com.

Manuscript received 4 Oct. 2010; revised 18 Apr. 2011; accepted 17 May 2011; published online 6 June 2011.

Recommended for acceptance by A. Okamura, C. Basdogan, S. Baillie, and W.S. Harwin.

For information on obtaining reprints of this article, please send e-mail to: toh@computer.org, and reference IEEECS Log Number THSI-2010-10-0086. Digital Object Identifier no. 10.1109/THSI.2011.34.

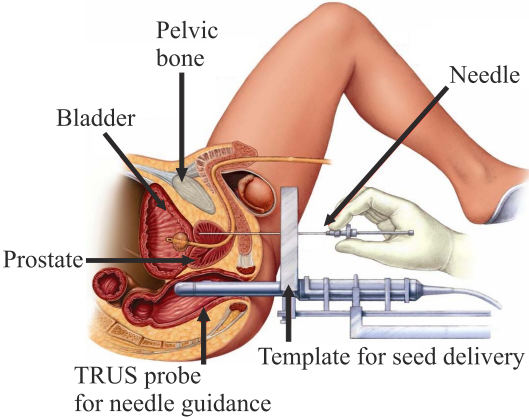


Fig. 1. In prostate brachytherapy, needles are inserted through a template to implant radioactive seeds at planned target locations. Brachytherapy is performed under the image guidance of transrectal ultrasound (TRUS), which is pressed against the prostate and hence also interacts with the pelvic anatomy.

ultrasound [12], and fluoroscopy [11] imaging. Data from needle insertions were collected during prostate brachytherapy for statistical modeling [10]. The latter insertion aspect, needle path modeling, was mainly studied for instrumented needle targeting. The needle path is affected by both lateral needle-tissue coupling due to flexible needle dynamics and the deflection of the needle path due to needle tip bevel. The coupling was often achieved using the FEM as a natural lateral constraint [13], [14], [16], [17], although simplified approaches were also proposed in order to achieve controllability of needle steering [15]. Beveled needle tips are commonly used for steering needles in tissue and, consequently, models were also proposed to simulate this effect [18], [19].

An early haptic simulation work on brachytherapy in [20] proposes a simple surface penetration based feedback. A one-dimensional (1D) haptic needle device using a similar interaction model was suggested in [21]. A heuristic model for prostate deformation and haptics was presented in [22]. Elaborate methods for FEM-based haptic simulation of needle insertion [14], [16], [23] and brachytherapy [17], [24] have also been studied in the literature. In this paper, we present a haptic brachytherapy simulator with simulated needle and probe interaction having validated needle flexibility and bevel models. A haptic simulation of this procedure complete with the modeling of the above-mentioned aspects has not been presented in the literature.

The paper is organized as follows: First, an overview of the methods is given in Section 2. Then, the simulation components relating to the needle and the probe are presented in Sections 3 and 4, respectively. Next, the integration of these components, the proposed optimizations for performance, and the haptic implementation are presented in Section 5. The results are reported in Section 6 and a discussion is provided in Section 7. Finally, Section 8 concludes the paper with a summary and plans for future work.

2 SIMULATOR OVERVIEW

In order to model tissue deformation, the FEM is employed with linear-geometry tetrahedra and linear stress-strain

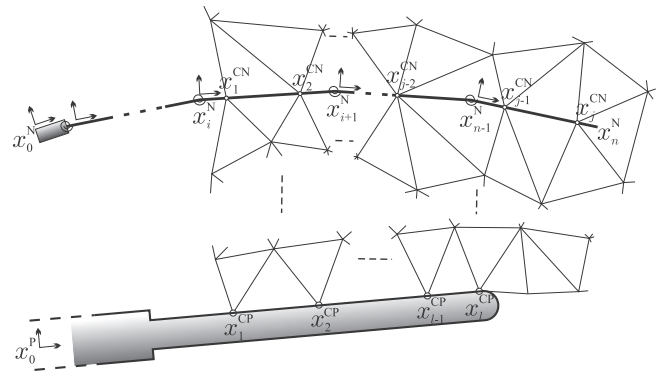


Fig. 2. Coupling of the discrete tissue model with the needle and probe models in the simulation.

assumption. Accordingly, the relation between the nodal displacements u and forces f of a discrete deformable tissue model (mesh) can be formulated using a stiffness matrix K as $f = Ku$. For given forces, a quasistatic solution for deformation can then be found by

$$u = K^{-1}f.$$

A detailed tissue model contains numerous nodes, thus the inverse stiffness matrix K^{-1} is a dense matrix of considerable size, making it difficult to solve the above system rapidly. Nonetheless, often only a small part of the model is in contact with instruments at any given time. Then, the relation between the nodal displacements u^c and forces f^c of such mesh *contact* nodes can be written using a much smaller (*condensed*) matrix K^c as follows [25]:

$$u^c = K^c f^c, \quad (1)$$

where K^c is formed by the elements of K^{-1} that correspond to the contact nodes. This is known as the *condensation method* and allows for simulations at fast (haptic) update rates.

Using low-rank *boundary condition change* and per-node frame rotation updates on K^c , mixed force/displacement boundary constraints can be applied on each individual node in a separate local coordinate frame [23]. Let the updated system matrix be K^w , the condensed *working* matrix, resulting in the following low-rank system:

$$b = K^w a, \quad (2)$$

where a is the vector of constraints and b is the vector of computed variables. Both vectors a and b may contain a combination of forces and displacements in individual coordinate frames at tissue *contact* nodes that are manipulated by medical instruments in our simulation. The following sections explain the constraints a and the processing of K^w in order to model tissue coupling to each instrument: the needle and the probe.

Fig. 2 illustrates the discrete tissue model (mesh) coupled to the needle and probe models. The probe is modeled as a rigid cylinder since its deformation is negligible, while the needle is thin and can bend significantly and therefore it is simulated using a 1D discrete flexible model with rigid rods connected by springs [26]. The user manipulates both virtual models via haptic devices, e.g., the base position x_0^N of the virtual needle is commanded via the interface,

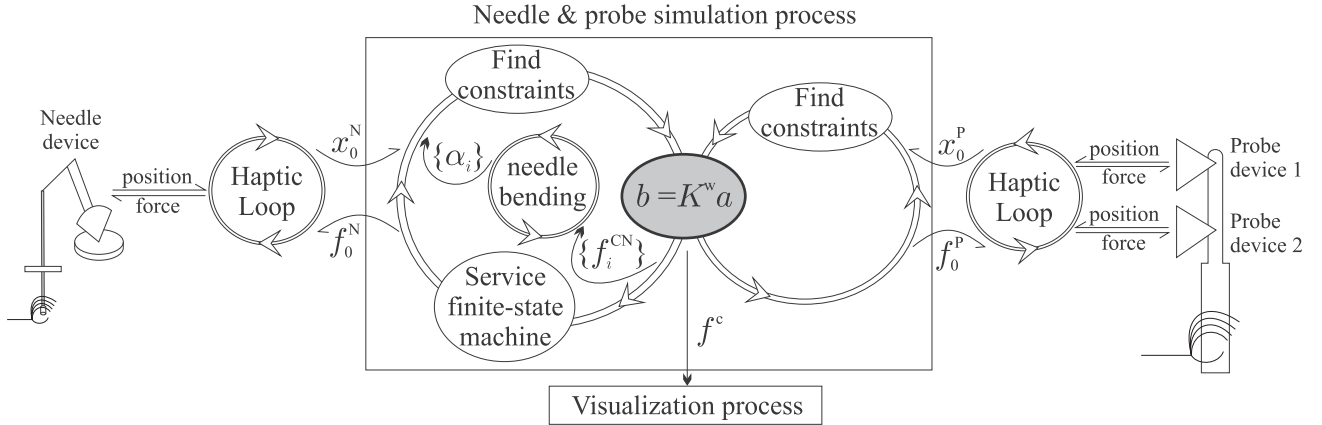


Fig. 3. Interaction between simulation components showing the dataflow of the following variables: the needle base position x_0^N and force feedback f_0^N , the TRUS probe position x_0^P and force feedback f_0^P , the needle bending angles $\{\alpha_i\}$, the forces on needle-tissue contact nodes $\{f_i^{CN}\}$, the forces on all contact nodes $f^c = \{f_i^{CN}, f_i^{CP}\}$, the vector of constraints a , the vector of computed variables b , and the low-rank (condensed) working matrix K^w . These are further explained in Section 2. The haptic process runs at high-priority whereas the visualization is performed as a lower priority task.

similarly to a physician manipulating a needle by holding it at its base. The model interaction occurs at the contact nodes of the tissue with the needle and the probe, positioned at $\{x_i^{CN}\}$ and $\{x_i^{CP}\}$, respectively. The reaction forces of the tissue at these contact nodes, $\{f_i^{CN}\}$ and $\{f_i^{CP}\}$, are then integrated at the haptic device location and are applied to the user's hand. These interaction forces further cause the needle to bend by changing its internal spring angles $\{\alpha_i\}$. Consequently, the needle configuration at any simulation instance is defined by the joint positions $\{x_i^N\}$ of the bent shaft in the reference frame of the needle base x_0^N .

Throughout this paper, $\{\cdot_i\}$ is used to refer to the set of vectors/variables where i takes all applicable values. Unless otherwise stated, x , f , and u denote position, force, and displacement vectors, respectively. For ease of representation, instrument base orientations and torques are included in the respective base position and force vectors, e.g., x_0^N denoting both the position and the orientation of the needle base.

Fig. 3 gives an overview of the simulation components and the data flow between them. The stick-slip model employed for a realistic haptic interaction of needle and tissue requires a finite state machine (FSM), which is serviced at each simulation iteration and updated when necessary. Preliminary results of this needle insertion simulation were previously presented in [27].

3 NEEDLE SIMULATION COMPONENTS

3.1 Simulation of Needle Insertion

Considering the physics of needle insertion, once the tissue is cut by the needle tip, the needle shaft is (laterally) confined to the *path* created by the advancing tip. In the axial direction, however, the needle encounters friction forces due to the grip of the tissue on the shaft surface. These two effects are modeled through corresponding axial force and lateral displacement constraints on contact nodes along the needle [9]. In addition to friction forces, the power required to cut the tissue at the needle tip imposes an additional resistance force to penetration. Accordingly, an axial force model is used where each tissue type can be

parameterized for a particular needle size/geometry by two constants: the *friction* force \hat{f}^F on shaft surface and the *tip* force \hat{f}^T required for cutting the tissue. Considering our 1D needle representation, \hat{f}^F has a unit of force-per-length which represents surface friction integrated around the shaft. \hat{f}^T is an (impulse) force at the tip and is only present during insertion, but not retraction. These parameters can be recovered experimentally for different needles and tissue types, following the methodology presented in [12] for a prostate phantom. The prostate and the perineum tissue models presented in this paper use the needle interaction parameters identified in that work.

Fig. 4 shows a sample force profile along the needle while it is being inserted in the prostate. For a given contact node position x_i^{CN} , let the distance of such a node from the needle base along the shaft be the scalar d_i . Then, the shaft-aligned component of this contact force f_i^{CN} can be defined as

$$f_{i,\text{shaft-aligned}}^{CN} = \pm \int_{d_i}^{d_{i+1}} \hat{f}_{\text{tissue}}^F, \quad (3)$$

where the sign depends on the motion direction, i.e., insertion or retraction. If the needle is advancing, an additional tip cutting force \hat{f}^T is imposed on the last needle contact node.

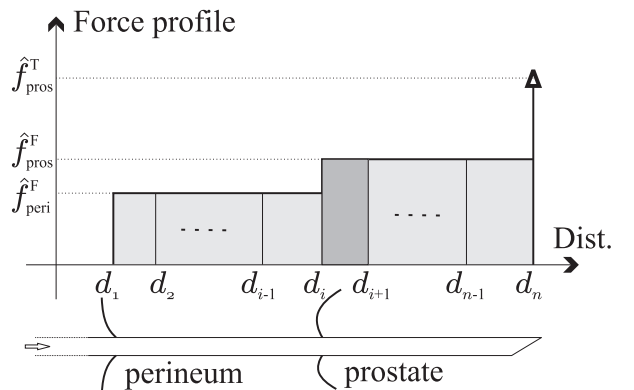


Fig. 4. Force profile model along the needle for shaft friction and tissue cutting at the tip, the latter of which is applied only during insertion.

A stick-slip friction model governs the needle-tissue contact [23]. The states $\{s_i\}$ of an FSM are updated for each needle contact node given the relative needle motion and the force constraints computed as described above. Accordingly, if the direction of needle travel changes, the axial force boundary constraint described above is switched to a displacement constraint, consequently fixing that particular contact node at its immediate location d_i on the shaft relative to the base. Assuming a static friction force (threshold) close to the dynamic friction force, the per-node integrated value above is also used as the threshold for a stuck-to-slipping state change. After FSM updates and aligning contact node coordinate frames with the needle shaft, boundary constraints a_i are enforced on these nodes depending on their states s_i .

Upon needle tip collision with the pelvic bone, a contact force is applied as a function of penetration depth. This simulates pubic arch interference, which occurs when anteriorly inserted needles hit the bone.

3.2 Simulation of Needle Flexibility

The flexible nature of the brachytherapy needle is simulated using an *angular springs* model, composed of a set of rigid rods connected by spring-loaded joints. These springs resist needle flexing and keep the shaft straight under a zero-load condition. This model was devised, parameterized, and validated for a brachytherapy needle in [26]. In this paper, contact forces $\{f_i^{\text{CN}}\}$ computed using the FEM for the tissue model are applied at each iteration along the shaft of this flexible needle model in order to find its bent shape.

Given the forces, the amount of rotation at each universal joint between the rigid links is found as follows: First, the aggregate torque τ_k of all forces located between this joint k and the needle tip (i.e., $\forall_{i>k} \{f_i^{\text{CN}}\}$) is computed. For linear angular springs, in static equilibrium the rotation of a joint is linearly proportional to the torque about its axis, i.e., $\tau_i = k \alpha_i$. This linearity constant k , the flexural modulus, was previously identified experimentally to be 10.7 Nmm/deg for a brachytherapy needle discretized at 1 cm intervals [26]. We assume that in brachytherapy needles, the torsion around the shaft axis is negligible. Thus, the tip bevel direction follows the roll angle of the needle base in our simulation.

3.3 Simulation of Needle Tip Bevel

Brachytherapy needles have a beveled tip allowing them to be steered. Steering may become necessary to avoid pubic arch interference, which is the partial occlusion of the anterior prostate region by the pelvic bone such that a straight-line insertion from the template cannot clear the pubic arch for the anterior-most seed targets. The oncologist can also utilize needle steering as a minor modification to the procedure plan to target a seed at a location that does not exactly align with a template hole. In fact, radiation oncologists regularly check the needle tip during insertion in the transversal ultrasound view. If the needle is advancing in an undesired direction, it is retracted (partially) and then reinserted with the tip bevel rotated to correct for this error. Therefore, modeling tip bevel is pertinent to brachytherapy simulation.

A model for simulating the bevel effect is devised based on the following observations on tissue-bevel interaction.

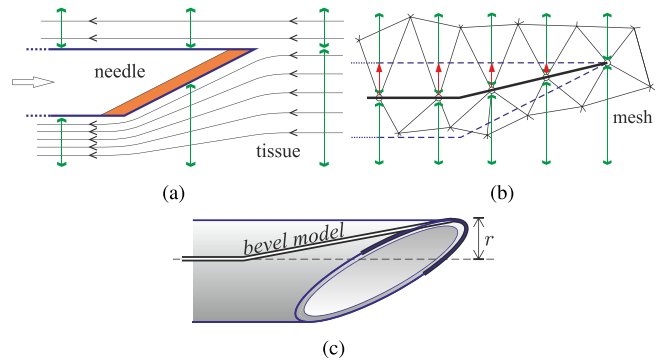


Fig. 5. (a) The progress of the beveled needle tip inside tissue; (b) mesh nodes sliding in 2D along a unidimensional tip-bevel model; and (c) tip-bevel model in 3D.

During needle insertion, the tissue is cut by the sharp edge of the tip and any tissue lying along the needle path is displaced to one side of the shaft by the beveled tip. This displaced tissue at an infinitesimal insertion instance is shown as shaded in 2D in Fig. 5a. Thus, as the needle advances, the tissue is effectively compressed on one side of the shaft, while the other side is unaffected. This results in an asymmetric force pushing the needle in the direction of the bevel (upward in Fig. 5a). As the needle is flexible, the shaft consequently bends thereby changing the insertion direction of the tip.

The above-mentioned asymmetric bevel effect can be simulated simply and effectively using the discrete 1D model described above in Section 3.2, by choosing this zero-thickness model (along which the tissue mesh nodes slide) as the cross-sectional centerline of the physical needle as seen in Fig. 5b. Consequently, as the needle advances, new contact nodes are issued at the tip of the bevel, where in fact the cut occurs and the tissue is split. The contact nodes then slide along the needle centerline, thereby effectively pulling the tissue nodes away from their nominal rest positions (downward in the figure). As a result, the internal tissue forces acting to bring the tissue mesh to its original position effectively creates a lateral tip force pushing the needle in the direction of the bevel. Note that this discrete model is consistent with the continuum case described above and seen in Fig. 5a in that: 1) the forces deflecting the needle indeed originate from the compression of tissue, which is simulated by the FEM in the discrete case, 2) the mechanism causing this compression is the tissue being forced to one side due to the beveled tip, and 3) tissue split occurs at the tip with penetration, which is ensured by our *remeshing* process that rediscretizes the tissue in order to obtain a mesh node precisely at the tip. It is easy to include this bevel tip model in our flexible shaft model by defining the beveled part of the centerline as a separate link. This bevel model originates from and was developed based on our earlier work on remeshing at the needle tip [24]. A similar bevel model was also presented in [17].

Although this bevel model replicates the continuum effect closely in 2D, some of the assumptions above need to be revisited for the 3D case. The main difference is that the cut (tissue split) in 3D does not happen at a single tip point alone as in 2D, but instead takes place around the sharp bevel rim seen in Fig. 5c. Also, since the cross-section is now

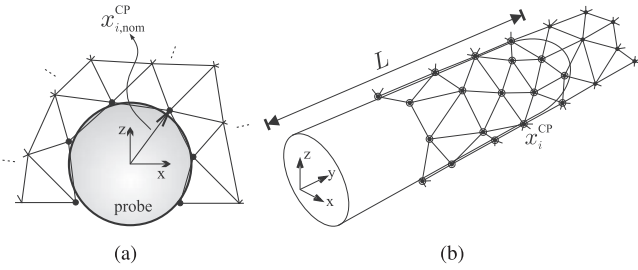


Fig. 6. (a) The positions $x_{i,nom}^{CP}$ of candidate probe contact nodes relative to the probe center axis in the undeformed nominal (segmented image) coordinate frame are recorded prior to simulation and (b) the contact nodes are determined during simulation from their distance to the probe base.

circular, there is no one single direction along which the displaced tissue is compressed as in 2D. Thus, a centerline model starting at the very tip may not create an accurate deflection in 3D. Nevertheless, a similar model in which the needle deflection is caused by an asymmetric force due to the compression of the sliding displaced tissue is also expected in 3D. Consequently, we devise a 3D model in which the deflection of the needle tip is defined by a bevel-tilt parameter r seen in Fig. 5c. This parameter is tuned experimentally as explained in Section 6.1. It has been identified as $r = 0.6$ mm for a standard brachytherapy needle, which has a radius of 0.64 mm.

4 TRUS PROBE SIMULATION COMPONENTS

Segmented TRUS images are used to generate a mesh model of the patient anatomy. The cylindrical probe surface, visible in these images, is also meshed separately to be used for the probe contact in the simulation. Note that during imaging the probe is in contact with the rectum and therefore the tissue mesh nodes on this segmented surface are part of the rectal wall and are accordingly the only nodes with which the probe can possibly interact in the simulation, in contrast to the needle which can be inserted at arbitrary locations. Furthermore, the majority of rectal wall nodes will be in constant contact with the probe as the probe resides in the rectum during the procedure. Therefore, to simulate the probe-tissue interaction, we use a different approach than that of the needle-tissue interaction, in which matrix elements corresponding to contact nodes

are added to and removed from the condensed system as the needle is manipulated. Because the list of *candidate contact nodes* forming the rectum is known a priori, the computational steps of addition/removal of contact nodes are avoided by forming the condensed matrix K^c for these candidate probe nodes prior to initiating the realtime haptic simulation. The relative positions $x_{i,nom}^{CP}$ of such candidate nodes with respect to the probe in the segmented image coordinate frame are also recorded initially as seen in Fig. 6a to be used in the simulation.

The probe surface physically poses a lateral displacement constraint on the tissue that it presses against. For axial probe translation inside the rectum, due to the lubrication of the balloon typically encapsulating the probe during procedures, a frictionless (sliding) contact is assumed tangentially on the probe surface. In the simulation, the nodes in contact with the probe are determined by using the y coordinates of their positions in the probe frame and the known probe geometry (length) as seen in Fig. 6b, e.g., $|x_0^P x_i^{CP}|_y < L$ suggesting contact. Based on this, one of the following constraints is applied in the probe coordinate frame:

$$\begin{cases} |f_i^{CP}|_y \leftarrow 0, |x_i^{CP}|_{x,z} \leftarrow |x_{i,nom}^{CP}|_{x,z}; & \text{if } i \text{ is in contact,} \\ |f_i^{CP}|_{x,y,z} \leftarrow 0; & \text{otherwise.} \end{cases}$$

5 HAPTIC COMPONENTS

5.1 Integration of Subsystems

A detailed flowchart of a simulation iteration is provided in Fig. 7. As can be seen, an impedance model of the environment is used, where the instrument positions are read and the forces on the haptic devices are computed. Certain variables are kept as the simulation states and updated accordingly. These variable include the angles α_i between the needle segments for the flexible needle model, the states $s_i \in \{\text{stuck}, \text{slipping}\}$ of needle contact nodes in the finite state machine responsible for the stick-slip friction model, and the contact node positions d_i on the needle shaft. Note that d_i is required both to compute the axial force profile described in Section 3 and also to propagate the location of a node *stuck* on the needle shaft between iterations. In order to ensure the stability of the coupled needle-tissue system, the

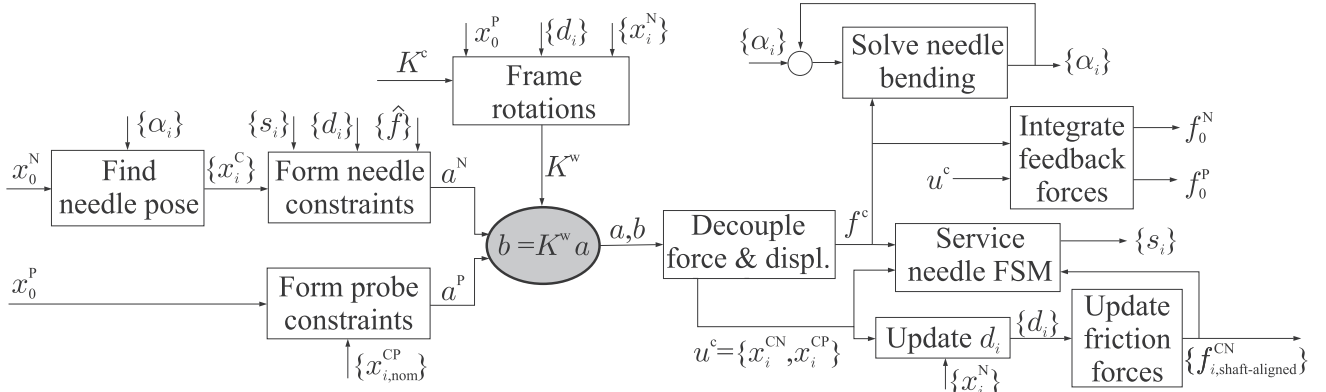


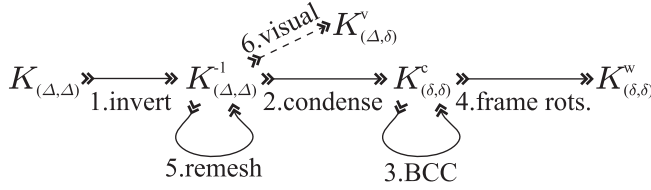
Fig. 7. Flowchart of an iteration showing major simulation operations and variables.

models of which are both deformable, the change in needle configuration $\{\alpha_i\}$ are damped. The changes in joint angles closer to the needle base cause a larger swing of the needle shaft and therefore the joint damping is set as a function of distance from the tip.

When the needle tip penetrates a new element in the tissue mesh, a contact node is added at the needle tip in order to ensure the conformity of the FEM mesh with the 1D needle model. For an accurate discretization of the tissue at that location, the tissue is locally remeshed on-the-fly [24]. During retraction, when the last contact node falls off the needle, i.e., $d_n > 20 \text{ cm}$, this node is removed from the condensed system K^c . Note that remeshing is not required for the probe since the rectal wall is segmented and meshed a priori.

In addition to haptic feedback, the simulation also computes mesh deformation given by $u = K^v f^c$, where K^v contains the columns of the inverted stiffness matrix corresponding to the contact nodes. A 3D view of the anatomy is then rendered by a separate low-priority process for visualization. This display includes deformed anatomical surfaces along with the needle, TRUS probe, and other visual cues that aid the comprehension of the layout in 3D.

The pipeline of the matrix updates performed through the simulation can be summarized as follows:



where the sizes of matrices are shown as subscripts. Δ is $(3 \times)$ the number of nodes in the entire FEM mesh and δ is $(3 \times)$ the number of contact nodes being interacted with, where $\Delta \gg \delta$. Each operation above can be summarized as follows:

1. In an offline step, the pelvic bone surface is set as the fundamental zero-displacement constraint and the resulting tissue stiffness matrix is inverted.
2. Elements corresponding to contact nodes are copied.
3. Low-rank updates are performed to switch between force and displacement boundary constraints. This operation is performed if a needle contact node changes its state or a probe contact is added or removed.
4. The local coordinate frame of each node is aligned with the desired constraints. This operation is performed for all contact nodes at each iteration.
5. Mesh modification is performed using one of the methods summarized below in Section 5.2.
6. The columns corresponding to the contact nodes are copied for the visualization process, where displacements are found from the nonzero contact forces f^c as $u = K^v f^c$.

Note that when a matrix is updated, the matrices that follow in the pipeline also need to be updated accordingly.

5.2 Performance Optimization

During the needle insertion, the tissue is remeshed to ensure compliance with the needle tip. The effect of changing the nominal position of any node can be reflected on the current

inverse tissue stiffness matrix K^{-1} by updating the matrix elements corresponding to this node and its immediate neighbors using the matrix inversion lemma [24]. Note that this is a full-rank matrix update and hence computationally intensive. Nevertheless, depending on the mesh size and the time that can be allowed for remeshing, this matrix update can be approximated at different levels of accuracy, thus trading off accuracy for speed. The implementation of the matrix inversion lemma, which allows for individual matrix elements to be updated independently, is exploited so that the elements are updated in the order of their importance. Such matrix elements are identified based on the following observations.

First, the change in K^{-1} will be concentrated on the rows/columns corresponding to the remeshed node j , the position of which is now changed relative to other tissue nodes. This can be seen intuitively by noting that such a position change mainly affects 1) the displacements inflicted on other nodes due to forces on j , and 2) the displacements observed on j due to forces on other nodes. Considering the relation $u = K^{-1}f$ between displacements and forces, these above effects relate to the rows/columns corresponding to node j .

Second, the mutual interaction between other nodes is not expected to change due to this modification of node position, since remeshing does not change the continuum material representation between other nodes. However, due to the discretization of tissue into finite elements, a small change may still occur in other K^{-1} rows/columns, in particular the ones corresponding to the immediate neighbors of node j .

Third and last, the change in K^{-1} is expected to be minimal even considering the entire matrix update, since the change in node position is likely to be relatively small with respect to model size and distances to boundaries. As a result, a potentially valid approximation is to not update the model at all. Alternatively, the time that can be feasibly permitted for remeshing can be allotted to the matrix elements where the change is most expected following the observations above, leading to the following list of four strategies:

- I. All elements of K^{-1} are updated.
- II. Only node j and its neighbors are updated in K^{-1} .
- III. Only node j is updated in K^{-1} .
- IV. K^{-1} is not updated.

One of the above strategies is chosen at the start of the simulation for a given mesh size and hardware processing power. This can also be modified in real time by the user for a desired trade-off between model detail, model accuracy, and haptic experience. The level of accuracy and the achieved speed gain are presented in Section 6.3. Accordingly, either method I or method III is used depending on the mesh size.

The matrix inversion lemma (step 5 in Section 5.1) is implemented on the graphics processing unit (GPU) using Nvidia CUDA libraries for improved performance. K^{-1} is loaded in the graphics device memory prior to the start of the simulation. If and when K^{-1} is changed, only the smaller condensed matrix K^c is compiled on the GPU and returned to the host memory (matrix update step 2 in Section 5.1).

5.3 Haptic Implementation

In brachytherapy, needles are inserted through template holes and the needle tip is steered in tissue by twisting the

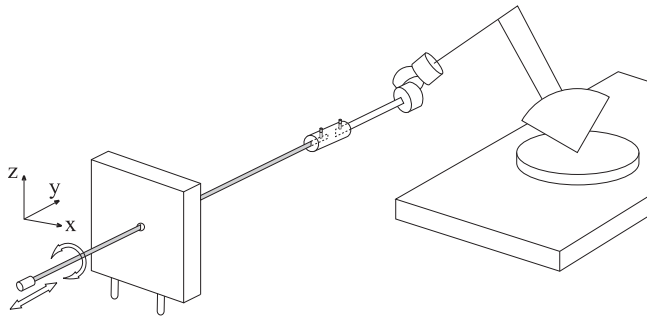


Fig. 8. The instrumentation of the haptic device on the brachytherapy needle.

base, which changes the orientation of the beveled tip. For simulating insertion, the device workspace needs to be larger than the maximum seed implant depth relative to the tissue surface. With additional margins to accommodate needles inserted slightly further and to allow a small range of motion outside the tissue, a workspace that allows a translation of 20 cm is required. In accordance with this design constraint, we have used a Sensable Phantom device instrumented with an actual brachytherapy needle inserted through a brachytherapy template as seen in Fig. 8. This gives the trainee a realistic interaction interface. The twist around the needle base is acquired by the last wrist encoder of the Phantom in order to command the tip bevel for steering.

In the simulation, the needle base position is inferred from the haptic device location, while the computed contact forces are integrated at the base of the needle model to be applied to the user's hand. The needle is controlled only along the insertion axis due to the constraint imposed by the template holes. Similarly, the force feedback is provided only along this axis. Accordingly, the haptic device is fixed in the lateral axes using a PID controller to align it with the physical template hole. For subsequent insertions at different template holes, such a location is chosen in the graphical user interface (GUI) once the needle is outside the patient. The virtual needle position is then moved laterally in the simulation to that template location, whereas the physical setup is left unchanged. This avoids complications that could arise, if the needle were allowed to be removed from the haptic device entirely. As a result, the same physical needle is used in our simulation to represent the needles of all 20–25 insertions of a typical brachytherapy procedure.

In brachytherapy, the TRUS probe is moved in the crano-caudal axis to image the entire prostate, which is typically less than 6 cm long. It is moved merely a couple of cm in the lateral directions for plan adjustments. Accordingly, allowing for 2 cm margin on either side, a 10 cm motion range for the probe is envisioned during the procedure. A mock probe instrumented with two Novint Falcon devices as depicted in Fig. 9a was devised to control the probe in the simulation. Each device has a 10 cm workspace in each axis and can provide over 9 N of force. The orientation of the probe is found from the relative positions of the devices.

Once the contact is simulated for a given probe location, the reaction forces of the tissue on the probe model are linearly distributed on each haptic device as in Fig. 9b. These are integrated for all contact forces and applied to the user.

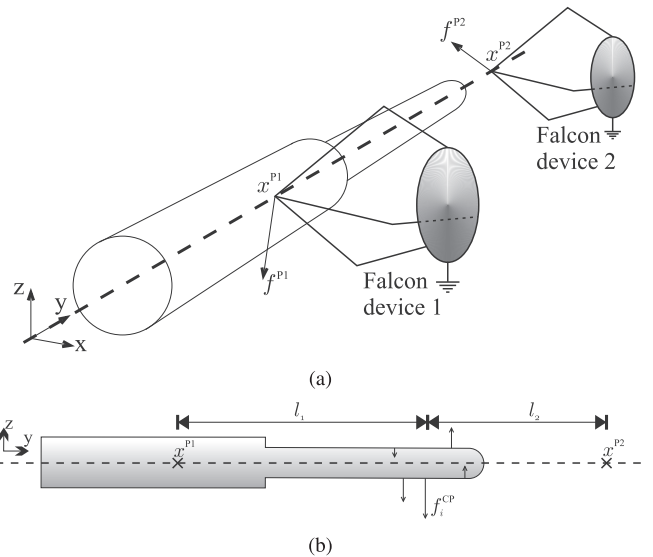


Fig. 9. (a) A mock TRUS-probe instrumented with Novint Falcon haptic devices and (b) the projection of the probe model forces onto the haptic devices.

The movement of the device is damped in the haptic loop to ensure stability.

6 RESULTS

6.1 Tip Bevel Simulation

In order to parameterize the tip bevel model, the following insertion experiment was designed. A brachytherapy needle was inserted into a clear PVC phantom through a template hole aligned with the phantom. A camera setup was used to observe the deflection of the needle due to the bevel. For the insertion, the needle bevel was pointed in a direction parallel to the phantom surface so that the deflection plane was perpendicular to the camera axis. A deflected needle is seen after an insertion in Fig. 10a. The tip deflection from the insertion axis shown in this figure is calculated using image processing.

This experimental setup is then modeled for our insertion simulation. Using the bevel model described in Section 3.3, simulated insertions with different bevel-tilt parameters r were performed under conditions similar to the experiment above. Fig. 10b demonstrates the bent needle after one such simulation. Fig. 10c shows the tip deflection as a function of base motion for four different values of r . The error between the tip deflections of the experimental insertion and the simulated insertions is minimized for r , yielding a bevel-tilt parameter $r \approx 0.6 \text{ mm}$ for the best fit of our model.

6.2 Interactive Simulation

Graphical and haptic user interfaces of our interactive simulator are seen in Fig. 11. The model on display generated from TRUS images is being manipulated with a Phantom-instrumented needle in Fig. 11a and a Falcon-instrumented mock probe in Fig. 11b. A detailed anatomical model generated from segmented MR images is seen in Fig. 12a. This model contains 3,278 nodes and 13,911 elements.

A close-up view of the anatomy during a sample needle insertion, during which the probe was also manipulated, is shown in Figs. 12b, 12c, 12d, and 12e. The movements of the needle base and of the probe are shown in Fig. 13a, where the

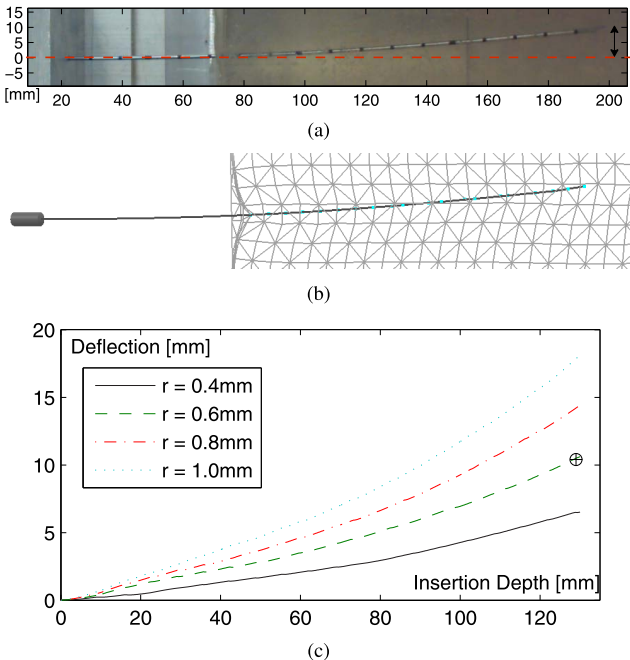


Fig. 10. (a) Needle insertion into a PVC phantom, showing the total amount of tip deflection due to tip bevel; (b) a simulated insertion using our tip bevel model into the FEM model of this phantom, with only the top surface mesh plotted; (c) tip deflection from the insertion axis for $r = 0.4, 0.6, 0.8, 1.0$ mm where the experimental tip deflection of 10.4 mm is also marked.

needle is inserted ($+y$) first, then the probe is advanced superiorly ($+y$) and moved anteriorly ($+z$), and finally the needle is retracted. The force feedback at the needle base recorded during this particular simulation is presented in Fig. 13b. The axial force is first seen to build up as the needle is advancing. When the probe is moved toward the needle compressing the tissue in-between, the lateral force on the needle base, which is held fixed, is observed to increase. Different force profiles of the perineum and the prostate due to different friction and cutting parameters are also seen during insertion and the retraction.

The time taken for each iteration of this simulated insertion is presented in Fig. 13c. The results are given with and without the probe-tissue interaction enabled in order to show the effect of additional probe contact nodes on the simulation speed due to increased condensed system size.

6.3 Remeshing Strategies

In Section 5.2, four methods are proposed for the remeshing operation for mesh adaptation enabling a

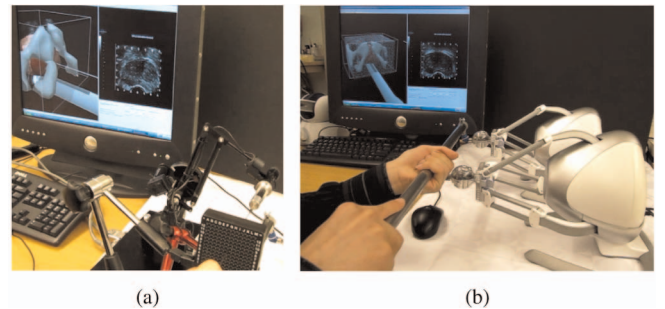


Fig. 11. (a) Needle insertion through template using a brachytherapy needle instrumented with a Sensable Phantom device, and (b) manipulation of a mock probe instrumented with two Novint Falcon devices.

trade-off between speed and accuracy. Method I is the original full-blown matrix operation. The other methods are approximations where accuracy is compromised compared to method I for different levels of acceleration. Here, the accuracy of methods III and IV are studied comparatively in terms of force feedback on the needle base and the position of the needle tip. The feedback force differences of the two methods from method I, taken as the gold-standard, are shown in Figs. 14a and 14b using the same insertion trajectory as in Fig. 13. This difference is the error introduced by switching to an alternative approximate remeshing strategy. A comparison of tip positions for all three methods is given in Fig. 14c.

Computation times taken by methods I and III are presented in Figs. 15a and 15b, respectively. A comparison of the GPU implementation using Nvidia CUDA and the CPU implementation using Intel MKL libraries is also provided in these figures. The results were generated on an Intel Core i7-870 (2.93 GHz) machine with 4 GB memory and an NVIDIA GeForce GTX 480 (1.5 GB) installed. The full matrix operation is seen to be accelerated 3-to-5 times with the use of the GPU. Furthermore, the processing time of the GPU is observed to be more deterministic between separate runs. The approximate remeshing method III involves a relatively smaller number of operations and thus does not yield a significant speed gain when performed on the GPU due to overheads such as memory transfers and kernel initiations.

The alternative remeshing method III is seen to run 10-to-50 times faster for this mesh size using either implementation. Furthermore, from Figs. 14a and 14c, where the results are almost identical to the full-blown remeshing method, it is seen that this acceleration comes

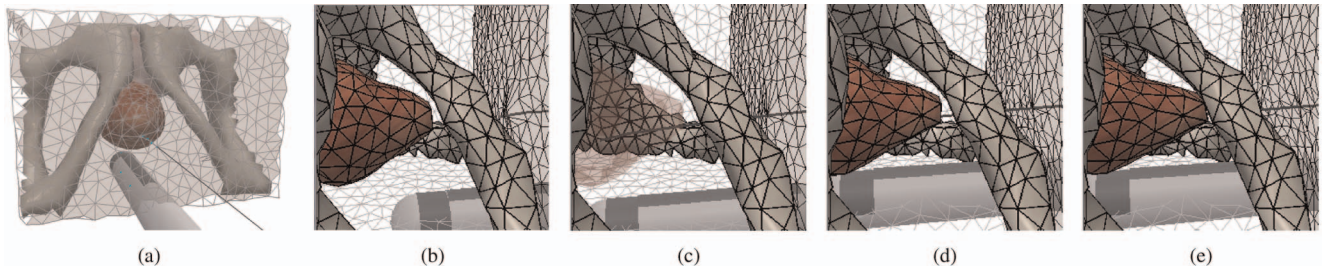


Fig. 12. An anatomical mesh view with the needle and the probe (a); and a close-up view of the prostate and the pelvic bone (b) while the needle is inserted, (c) when the needle reached its target (the prostate is shown transparent here for better needle visibility) and the probe is inserted further, (d) after which the probe is adjusted by moving it anteriorly (upward in this image), and (e) during needle retraction.

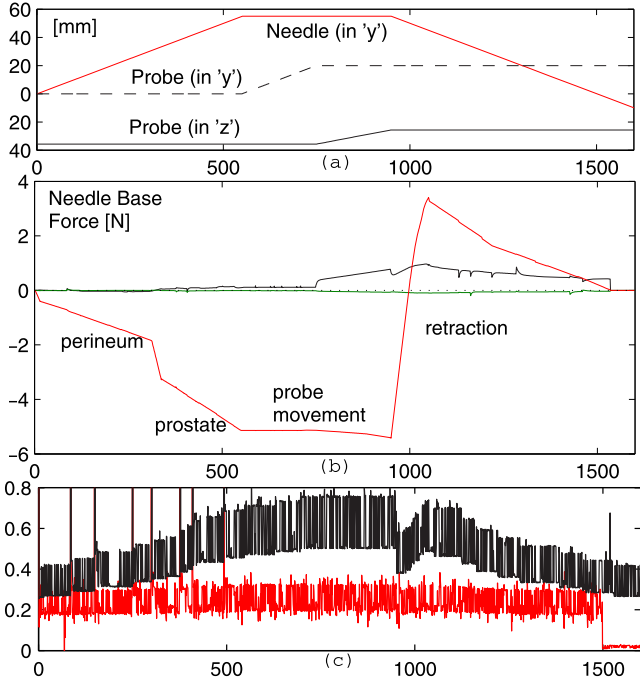


Fig. 13. (a) Needle and probe paths as an interaction example: only the axes with motion are plotted (needle in y and probe in x) with initial position as the origin. (b) Forces at the needle base, where the insertion forces are seen and the lateral force is observed to build up due to the displaced tissue as the probe moves toward the needle. (c) The time taken for each simulation iteration for this sample insertion is presented with and without the probe-tissue interaction enabled. When disabled, the simulation runs faster due to the smaller condensed system. The peaks occurring during needle insertion that exceed the plot axis limits are due to tissue remeshing. The time taken for those are reported and discussed in Fig. 15 and Section 6.3, respectively.

at little or no expense in terms of accuracy. Therefore, method III is employed with large meshes in our realtime implementation.

7 DISCUSSION

The needle instrumentation passing through a template was devised to mimic the actual procedure and to give the trainee an operating-room like interaction interface. Together with the GUI, the instrumented needle allows for carrying out the needle insertions of an entire brachytherapy procedure plan. Should the trainee reach behind the template to bend the needle, as it is sometimes done during actual procedures, it will be a simple modification to monitor the Phantom device lateral motion relative to the needle insertion axis in order to use this as a force sensor and bend the virtual needle accordingly.

The simulator also allows insertions to be performed without the template constraint, so needle manipulation and force feedback will exist in all axes. The probe and the needle can furthermore be controlled using the GUI, keyboard interface, or a precomputed path file. This allows for a haptic simulation of either the needle or the probe alone.

Obtaining a mesh model of a desired anatomical region with a mesh size suitable for interactive haptic simulation can be challenging. This is often performed by first segmenting medical images, followed by tessellating them using common meshing tools from the mechanical engineering literature. In [28], we introduced a meshing

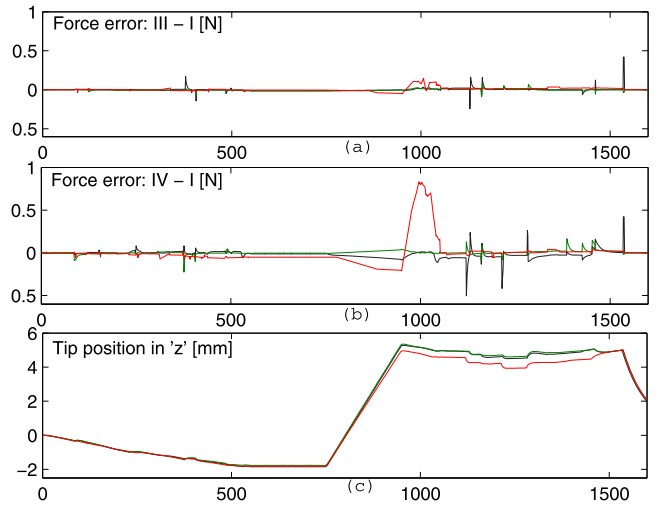


Fig. 14. Error in needle base feedback force when remeshing is carried out using (a) method III and (b) method IV, compared to the gold-standard data from the full-blown method I. (c) The position of the needle tip when using methods I, III, and IV. Only the (anterior) z -axis components, where the major changes occur, are shown. Methods I and III are seen to be closely matched, whereas method IV differs slightly, especially after the probe movement.

technique for medical images by incorporating the segmentation task into the meshing process itself. It allows for defining a node budget and generates optimal meshes to discretize images given that budget. Therefore, this method is particularly beneficial in generating low-order anatomical meshes for haptic interaction.

As seen in Fig. 15, remeshing method I benefits from a GPU implementation as the matrix-inversion-lemma is performed in multiple threads concurrently. However, to update a smaller part of the matrix, the setup overhead (thread initialization and data transfer) is very large relative to the computation itself. Therefore, method III does not gain much from the GPU implementation. As expected, the computer hardware can play a major role in achieving high sampling rates for haptic simulation. For instance, the presented setup runs remeshing tests an

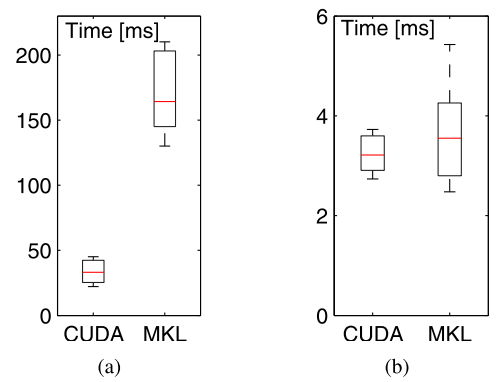


Fig. 15. The time taken by remeshing for the detailed patient model using (a) method I and (b) method III. Because of the nondeterministic behavior of the nonrealtime operating system and the difference in number of neighbors each node remeshing involves, processing time is reported as a statistical bar plot, where the median, quartiles, and the extent of data are shown. A comparison of Nvidia CUDA and Intel MKL implementations are also presented in these figures. Note that method IV does not require any computation and therefore it is not reported in this figure.

average of three times faster compared to a slower test platform (Intel dual-core processor with Nvidia GTS 250) in an earlier development iteration. The least speed gain with this faster hardware was observed for the GPU implementation of method III, the bottleneck of which is not the computation, but the setup overhead.

When a new mesh element is penetrated by the needle tip, one of the four corners of this element is picked for remeshing. Each corner in turn is temporarily moved to the needle tip and the Jacobian of each modified neighbor tetrahedron is computed. The worst condition number [29] of these neighboring tetrahedra is assigned as the geometric-quality cost of remeshing this node. Accordingly, the corner node with the best cost is selected for remeshing.

Note that remeshing via method IV is different from the *node snapping* performed in [23], where nodes are forced on the needle from their nominal locations. Using node snapping, large lateral forces are generated that both destabilize a flexible needle and artificially bend it in the snapped direction. In contrast, using method IV the node location is redefined to be at the new remeshed location, while the stiffness representation K^{-1} is left unchanged. This is effectively equivalent to projecting constraints from *virtual* contact nodes that reside on the needle onto actual tissue mesh nodes.

As seen in Figs. 14b and 14c, larger force errors and a tip position error of up to 0.5 mm are observed with method IV. Nevertheless, these errors occur only after *lateral* probe motion, for which the local mesh between the needle and the probe is of greater significance. Although corrections to probe placement are common between needle insertions, moving the probe laterally while the needle is inserted is not a common practice in brachytherapy. All the same, such probe corrections *between* insertions still deform the tissue changing the anatomy, and hence also the force feedback caused by a subsequent insertion at the same location. Consequently, the resulting seed implant location will also differ. Therefore, simulating deformations due to the TRUS probe is essential. The demonstration of radial probe movement while the needle is inserted is merely a choice of presentation for the purposes of this haptics paper and to better display the force coupling between these instruments through the deformable soft tissue model. Although method IV is *not* used in our simulation based on our accuracy analysis, considering radial probe motion (corrections) only between insertions this method may not be as detrimental for the simulation and may still be the method of choice in situations where lesser accuracy is acceptable.

In this paper, the same underlying methods for handling contact constraints is utilized for both the needle and the TRUS probe. Nonetheless, due to the different nature of their actual physical interaction with tissue, separate constraint models have been developed for each. Furthermore, it has been demonstrated that the two instrument models can run in a plausible simulation using the given framework and a realistic range of biomechanics parameters while both models are connected through a deformable tissue FEM model, are manipulated using three haptic devices in total, and one of the models (the needle) is internally flexible.

To overcome memory transfer bottlenecks in the GPU implementation, asynchronous operations are preferred whenever possible. Similarly, the variables of the data flow

between processes in the simulation are not locked for access unless necessary. For instance, the realtime process can be updating the displacements at the same time as the visualization process uses them for display. This may result in two different parts of the mesh containing displacements from subsequent iterations, which is not a problem because the change in displacements is marginal between iterations of the simulation.

As seen in Fig. 14c, the simulation rate is bounded by the size of the condensed system. In addition to the number of contact nodes added on the needle during insertion, the number of candidate contact nodes allocated for the probe is a major factor that affects the simulation speed. To that end, assuming a densely located set of nodes on the virtual probe surface, a spatially downsampled subset can be assigned as the candidate contact nodes such as by simply picking every n th node axially. This effectively creates a looser probe-tissue coupling in-between such downsampled candidate nodes, with a significant gain in speed. A downsampling of two is used for the results in this figure yielding 22 candidate nodes.

In our training simulator, the anatomical surfaces are typically displayed with texture and lighting. Mesh elements are depicted in the figures of this paper to better demonstrate the underlying mesh size and behavior. Simulated TRUS images are also seen in the GUI. This simulation aspect is not the focus of this paper and will be presented elsewhere.

8 CONCLUSIONS

A haptic simulator of the prostate brachytherapy procedure has been presented in this paper. Brachytherapy needles bend due to their flexible shaft and deflect during insertion due to their tip-bevel. Models to account for both of these effects have been presented. The interaction of the TRUS probe with the tissue, an integral part of the brachytherapy procedure, has also been modeled. The manipulation of the needle and the probe have been implemented on haptic devices and demonstrated in this paper. This is the first haptic interaction model in the literature for prostate brachytherapy with deformable tissue, flexible needle, needle deflection based on bevel action, and a model of the ultrasound transducer—all the features necessary for a realistic simulation encompassing the major effects affecting the accurate delivery of radiation sources. The pertinent computational acceleration aspects that allowed for the simulation of the needle-tissue and ultrasound probe-tissue interaction at refresh rates that are suitable for haptic interaction have been described.

In future studies, the simulator performance will be characterized based on feedback from expert physicians. Intraoperative results of needle insertion and probe manipulation in patients will be compared with those obtained in patient-specific models by comparing the resulting of actual prostate motion with that of the virtual prostate motion.

ACKNOWLEDGMENTS

The authors would like to thank the National Sciences and Engineering Research Council (NSERC) of Canada for the financial support of this work.

REFERENCES

- [1] S. Langley and R. Laing, "Prostate Brachytherapy Has Come of Age: A Review of the Technique and Results," *British J. Urology Int'l*, vol. 89, pp. 241-249, 2002.
- [2] E.P. Westerbrink-van der Putten, R.H.M. Goossens, J.J. Jakimowicz, and J. Dankelman, "Haptics in Minimally Invasive Surgery—A Review," *Minimally Invasive Therapy and Allied Technologies*, vol. 17, no. 1, pp. 3-16, 2008.
- [3] Simbionix. <http://www.simbionix.com/>, 2011.
- [4] CAE Healthcare, <http://www.cae.com/>, 2011.
- [5] N. Famaey and J.V. Sloten, "Soft Tissue Modelling for Applications in Virtual Surgery and Surgical Robotics," *Computer Methods in Biomechanics and Biomedical Eng.*, vol. 11, no. 4, pp. 351-366, 2008.
- [6] S. Misra, K.T. Ramesh, and A.M. Okamura, "Modeling of Tool-Tissue Interactions for Computer-Based Surgical Simulation: A Literature Review," *Presence: Teleoperators and Virtual Environments*, vol. 17, no. 5, pp. 463-491, 2008.
- [7] N. Abolhassani, R. Patel, and M. Moallem, "Needle Insertion into Soft Tissue: A Survey," *Medical Eng. Physics*, vol. 29, pp. 413-431, 2007.
- [8] A. Okamura, C. Simone, and M. O'Leary, "Force Modeling for Needle Insertion Into Soft Tissue," *IEEE Trans. Biomedical Eng.*, vol. 51, no. 10, pp. 1707-1716, 2004.
- [9] S.P. DiMaio and S.E. Salcudean, "Needle Insertion Modeling and Simulation," *IEEE Trans. Robotics and Automation*, vol. 19, no. 5, pp. 864-875, 2003.
- [10] T. Podder et al., "In Vivo Motion and Force Measurement of Surgical Needle Intervention during Prostate Brachytherapy," *Medical Physics*, vol. 33, no. 8, pp. 2915-2922, 2006.
- [11] J. Hing, A. Brooks, and J. Desai, "Reality-Based Estimation of Needle and Soft-Tissue Interaction for Accurate Haptic Feedback in Prostate Brachytherapy Simulation," *STAR Robotics Research*, vol. 28, pp. 34-48, 2007.
- [12] E. Dehghan, X. Wen, R. Zahiri-Azar, M. Marchal, and S.E. Salcudean, "Needle-Tissue Interaction Modeling Using Ultrasound-Based Motion Estimation: Phantom Study," *Computer Aided Surgery*, vol. 13, no. 5, pp. 265-280, 2008.
- [13] S.P. DiMaio and S.E. Salcudean, "Needle Steering and Motion Planning in Soft Tissues," *IEEE Trans. Biomedical Eng.*, vol. 52, no. 6, pp. 965-974, 2005.
- [14] R. Alterovitz, M. Branicky, and K. Goldberg, "Motion Planning under Uncertainty for Image-Guided Medical Needle Steering," *Int'l J. Robotics Research*, vol. 27, pp. 1361-1374, 2008.
- [15] D. Glotzman and M. Shoham, "Flexible Needle Steering for Percutaneous Therapies," *Computer Aided Surgery*, vol. 11, no. 4, pp. 194-201, 2006.
- [16] C. Duriez, C. Guébert, M. Marchal, S. Cotin, and L. Grisoni, "Interactive Simulation of Flexible Needle Insertions Based on Constraint Models," *Proc. 12th Int'l Conf. Medical Image Computing and Computer Assisted Intervention (MICCAI '09)*, pp. 291-299, 2009.
- [17] N. Chentanez, R. Alterovitz, D. Ritchie, L. Cho, K.K. Hauser, K. Goldberg, J.R. Shewchuk, and J.F. O'Brien, "Interactive Simulation of Surgical Needle Insertion and Steering," *ACM Trans. Graphics*, vol. 28, no. 3, pp. 1-10, 2009.
- [18] H. Kataoka, T. Washio, K. Chinzei, and K. Mizuhara, "A Model for Relations between Needle Deflection, Force, and Thickness on Needle Penetration," *Proc. Fourth Int'l Conf. Medical Image Computing and Computer-Assisted Intervention (MICCAI '01)*, pp. 966-974, 2001.
- [19] R.J. WebsterIII, J.S. Kim, N.J. Cowan, G. Chirikjian, and A.M. Okamura, "Nonholonomic Modeling of Needle Steering," *Int'l J. Robotics Research*, vol. 25, pp. 509-525, 2006.
- [20] A. Kimura, J. Camp, R. Robb, and B. Davis, "A Prostate Brachytherapy Training Rehearsal System—Simulation of Deformable Needle Insertion," *Proc. Fifth Int'l Conf. Medical Image Computing and Computer Assisted Intervention (MICCAI '02)*, pp. 264-271, 2002.
- [21] A. Okrainec, M. Farcaș, O. Henao, I. Choy, J. Green, M. Fotoohi, R. Leslie, D. Wight, P. Karam, N. Gonzalez, and J. Apkarian, "Development of a Virtual Reality Haptic Veress Needle Insertion Simulator for Surgical Skills Training," *Proc. Medicine Meets Virtual Reality*, pp. 233-238, 2009.
- [22] X. Wang and A. Fenster, "A Virtual Reality Based 3D Real-Time Interactive Brachytherapy Simulation of Needle Insertion and Seed Implantation," *Proc. IEEE Int'l Symp. Biomedical Imaging: Nano to Macro*, pp. 280-283, 2004.
- [23] S.P. DiMaio and S.E. Salcudean, "Interactive Simulation of Needle Insertion Models," *IEEE Trans. Biomedical Eng.*, vol. 52, no. 7, pp. 1167-1179, 2005.
- [24] O. Goksel, S.E. Salcudean, and S.P. DiMaio, "3D Simulation of Needle-Tissue Interaction with Application to Prostate Brachytherapy," *Computer Aided Surgery*, vol. 11, no. 6, pp. 279-288, 2006.
- [25] M. Bro-Nielsen and S. Cotin, "Real-Time Volumetric Deformable Models for Surgery Simulation Using Finite Elements and Condensation," *Computer Graphics Forum (Eurographics)*, vol. 15, no. 3, pp. 57-66, 1996.
- [26] O. Goksel, E. Dehghan, and S.E. Salcudean, "Modeling and Simulation of Flexible Needles," *Medical Eng. and Physics*, vol. 31, no. 9, pp. 1069-1078, 2009.
- [27] O. Goksel and S.E. Salcudean, "Haptic Simulator for Prostate Brachytherapy with Simulated Ultrasound," *Proc. Int'l Symp. Biomedical Simulation (ISBMS)*, pp. 150-159, 2010.
- [28] O. Goksel and S.E. Salcudean, "Image-Based Variational Meshing," *IEEE Trans. Medical Imaging*, vol. 30, no. 1, pp. 11-21, 2011.
- [29] L.A. Freitag and P.M. Knupp, "Tetrahedral Mesh Improvement via Optimization of the Element Condition Number," *Int'l J. Numerical Methods in Eng.*, vol. 53, pp. 1377-1391, 2002.



Orcun Goksel (S'00-M'10) received the BSc degrees in electrical engineering in 2001 and in computer engineering/science in 2002, both from the Middle East Technical University, Ankara, Turkey. He received the MSc and PhD degrees in electrical and computer engineering at the University of British Columbia, Vancouver, BC, Canada, in 2004 and 2009, respectively. He is currently a postdoctoral fellow at the University of British Columbia, Vancouver, BC, Canada. His research interests include elastography, patient model generation, medical simulations, haptics, and image guided therapy. He is a member of the IEEE.



Kirill Sapchuk is currently working toward the BSc degree in computer science and physics at the University of British Columbia, Vancouver, BC, Canada. He has worked in the Department of Electrical and Computer Engineering on mesh generation for medical applications and ultrasound image simulation. His research interests include medical simulation and high performance computing. He is a student member of the IEEE.



Septimiu E. Salcudean (S'78-M'79-SM'03-F'05) received the BEng and MEng degrees from McGill University and the PhD degree from U.C. Berkeley, all in electrical engineering. From 1986 to 1989, he was a research staff member in the robotics group at the IBM T.J. Watson Research Center. He then joined the Department of Electrical and Computer Engineering at the University of British Columbia, Vancouver, Canada, where he is now a C.A. Laszlo professor of Biomedical Engineering and holds a Canada research chair. He spent one year at ONERA-CERT (aerospace-controls laboratory) in Toulouse, France, in 1996 to 1997, where he held a Killam research fellowship, and six months, during 2005, in the medical robotics group (GMCAO) at CNRS in Grenoble, France. He is interested in medical robotics and ultrasound image guidance, elastography, haptic interfaces, and virtual environments. He has been a co-organizer of several symposia on haptic interfaces and a technical and senior editor of the *IEEE Transactions on Robotics and Automation*. He is a fellow of the IEEE and the Canadian Academy of Engineering.

▷ For more information on this or any other computing topic, please visit our Digital Library at www.computer.org/publications/dlib.